International Journal of Thermal Sciences 213 (2025) 109790

Contents lists available at ScienceDirect

International Journal of Thermal Sciences

journal homepage: www.elsevier.com/locate/ijts

Advancing thermal radiation efficiency with hybrid-patterned metasurface emitters in thermophotovoltaic systems

Ting Cai [a], Zhiheng Xu [a,b,*], Yujie Yi [a], Chen Wang [a], Baisong Zhou [a], Chao Chen [a], Yunpeng Liu [a,b], Yuqiao Wang [c], Hongbo Lu [d], Xiaobin Tang [a,b,**]

[a] Department of Nuclear Science and Technology, Nanjing University of Aeronautics and Astronautics, Nanjing, 210016, China
[b] Key Laboratory of Advanced Nuclear Technology and Radiation Protection, Ministry of Industry and Information Technology, Nanjing, 211106, China
[c] Research Center for Nano Photoelectrochemistry and Devices, School of Chemistry and Chemical Engineering, Southeast University, Nanjing, 211189, China
[d] State Key Laboratory of Space Power, Shanghai Institute of Space Power-sources, Shanghai, 200245, China

ARTICLE INFO

Keywords:
Thermophotovoltaic system
Hybrid-patterned metasurface emitter
Deep learning
Thermal radiation
Effective spectral efficiency

ABSTRACT

In thermophotovoltaic systems, it is essential for emitters to effectively convert thermal energy into thermal radiation photons within the useable wavelengths for photovoltaic cells. Metasurface emitters enable broadband emission to efficiently and accurately match photovoltaic cells because of their complex optical properties and adjustable resonance behavior. In this study, a hybrid-patterned metasurface emitter was designed using an inverse neural network and optimized by a genetic algorithm to efficiently match InGaAs cells with different bandgaps. The designed hybrid-patterned metasurface emitter exhibits 90% high in-band emission with near-zero out-of-band emission, and it is angle insensitive and polarization independent. The optical performance of the emitter and the output performance of the radioisotope thermophotovoltaic system were studied at temperatures ranging from 700 K to 1300 K. At 1300 K, the emitter demonstrates an effective spectral efficiency of 69.84%. The radioisotope thermophotovoltaic system with a 0.56 eV InGaAs cell has a maximum output power density of 1.16 W/cm^2 and an energy conversion efficiency of 20.77%. The mechanism of selective emission was elucidated. Finally, the hybrid-patterned metasurface emitter was fabricated by micro-nano fabrication technology, and its performance was studied. The optimization and fabrication of the hybrid-patterned metasurface emitter provide an important theoretical foundation and practical guidance for enhancing thermal radiation efficiency.

Nomenclature

R	radius of the circle (nm)
L	side length of the square (nm)
A	period of the hybrid pattern (nm)
D	distance of the circle and square (nm)
h_1	thickness of the pattern W layer (nm)
h_2	thickness of the Al_2O_3 layer (nm)
h_3	thickness of the bottom W layer (nm)
λ	wavelength (nm)
ε	emissivity of object (%)
α	absorptivity of object (%)
r	reflectance of object (%)
I_{em}	radiant power of emitter (W/m^2·nm)
I_{BB}	radiant power of Blackbody (W/m^2·nm)
T	temperature (K)
h	Planck's constant
c	speed of light in a vacuum (m/s)
k_B	Boltzmann's constant
η_{sp}	effective spectral efficiency of emitter (%)
λ_{PV}	cut-off wavelength of PV cell (nm)
J	output current density of PV cell (A/cm^2)
J_{sc}	short-circuit current density of PV cell (A/cm^2)
J_0	inverse saturation current density of PV cell (A/cm^2)
QE	quantum efficiency of PV cell (%)
E_g	bandgap of PV cell (eV)
T_a	ambient temperature of PV cell (K)
V	output voltage (V)
q	elementary charge (C)
P_{max}	maximum output power density (W/cm^2)
η_{sys}	energy conversion efficiency (%)

---

* Corresponding author. Department of Nuclear Science and Technology, Nanjing University of Aeronautics and Astronautics, Nanjing, 211106, China.
** Corresponding author. Department of Nuclear Science and Technology, Nanjing University of Aeronautics and Astronautics, Nanjing, 211106, China.
E-mail addresses: xuzhiheng@nuaa.edu.cn (Z. Xu), tangxiaobin@nuaa.edu.cn (X. Tang).

https://doi.org/10.1016/j.ijthermalsci.2025.109790
Received 11 October 2024; Received in revised form 23 January 2025; Accepted 10 February 2025

Abbreviations

RTPV	radioisotope thermophotovoltaic
PV	photovoltaic
FDTD	finite-difference time-domain
MIM	metal-insulator-metal
W	tungsten
Al_2O_3	aluminum oxide
Si	silicon
SiO_2	silicon dioxide
MSE	mean squared error
InGaAs	indium gallium arsenic
PMMA	polymethyl methacrylate

1. Introduction

Thermophotovoltaic (TPV) systems convert thermal radiation from heat sources into electrical energy through the photovoltaic effect, which have high power density, and energy conversion efficiency. These heat sources include nuclear energy, solar energy, hydrocarbon fuels, and industrial waste heat. Notably, radioisotope thermophotovoltaic (RTPV) systems that leverage radioisotope decay heat exhibit extended operational lifespans and enhanced stability. Since the proposal of this type of power supply, researchers have been committed to achieving high-power, efficiency, and reliability combination designs through techniques such as spectral control and system construction [1–5]. Therefore, the RTPV system is regarded as an important energy technology for future space exploration, which can contribute to the sustainable development of space science [6–8].

During energy conversion of RTPV systems, only radiation photons above the bandgap energy of the photovoltaic (PV) cell, referred to as the "in-band" portion, can be utilized by the PV cell to convert into electrical energy. Radiation photons below the bandgap energy, referred to as the "out-of-band" portion, cannot be converted but may heat the PV cells, leading to performance degradation. Most of the thermal radiation occurs over a relatively long broad spectrum, resulting in considerable energy waste. Therefore, maximizing the in-band emission and suppressing the out-of-band emission of the emitters through specific spectral control are effective ways to improve the output performance and stability of the system.

Early emitters typically used materials with inherent optical selection properties such as rare-earth oxides [9,10] or metal-doped ceramics [11] to achieve spectral control. However, these spectra often exhibit narrow-band emissions, and the peak position is difficult to adjust [12]. With the development of nanophotonics and micro-nano processing technologies, research on selective emitters based on structural control of spectral properties has gradually emerged, including diffraction gratings [13,14], photonic crystals [15–17], and metamaterials [18–24]. Metamaterials have attracted considerable attention in emission regulation because of their high-precision adjustable resonance behavior [25–28]. Previous studies have shown that arranging multiple patterns of different sizes in one period can achieve a specific range of multi-peak and broadband absorption/emission effects [23,29–31]. However, the increase in parameters inevitably leads to a large number of possible candidate structures, and theoretical calculation methods such as finite-difference time-domain (FDTD) iteration to calculate the optical properties of corresponding metamaterial structures require substantial computation and time costs. In recent years, the development of artificial intelligence has provided new ideas for optimizing selective emitters [32–35]. Deep learning models have been proven to effectively characterize the physical relationship between multi-dimensional photonic structures and their optical properties in the design of photonic devices [36,37]. Therefore, optimizing emitters with deep learning has great application potential, especially in exploring the nonlinear relationship between complex structures and optical properties.

In this work, a hybrid-patterned metasurface emitter was designed using deep learning in combination with a genetic algorithm to match the InGaAs cells in RTPV systems. The designed emitter exhibits high in-band broadband emission with nearly zero out-of-band emission, and it is angle-insensitive and polarization-independent. Meanwhile, the physical mechanisms and the gain of the designed emitter to the RTPV system at different temperatures were discussed. In addition, the designed emitter was fabricated using advanced micro-nano manufacturing techniques. The experimental results indicate that the emitter possesses selective emission characteristics, making it well-suited to match the response band of the 0.56 eV InGaAs cell.

2. Materials and methods

2.1. Ideal emissivity optimization

The quantum efficiency of customized InGaAs cells with bandgaps of 0.68 eV, 0.56 eV, and 0.50 eV was measured by the QE-R measurement system (FYL-YS-50LK). To achieve the optimal performance of these InGaAs cells, the emissivity spectrum of the emitter was tailored on the basis of their specific bandgaps. As shown in Fig. 1, the ideal emissivity spectrum was defined by maximizing the in-band emission (emissivity set to 1) and minimizing the out-of-band emission (emissivity set to 0). The ideal emission spectrum served as the target spectrum for prediction. Then, the corresponding quantum efficiency data were used to evaluate the overall performance improvement of the RTPV system.

The schematic diagram of the emitter based on the metal-insulator-metal (MIM) structure is shown in Fig. 2. This structure consists of three layers of tungsten (W), aluminum oxide (Al_2O_3), and W. Each period is composed of symmetrical circular and square patterns, with resonance frequencies adjusted to achieve broadband emission. The geometric parameters of the emitter include the radius of the circle R, the side length of the square L, the period of the hybrid pattern A, the distance between the circle and square D, the thickness of the pattern W layer h_1, the thickness of the Al_2O_3 layer h_2, and the thickness of the bottom W layer h_3.

The FDTD method was employed to simulate the interaction between electromagnetic waves and the hybrid-patterned metasurface. Frequency-domain field monitors were placed to obtain the characteristic spectrum in the range of 0.3–6.0 μm at the micro–nano scale. According to Kirchhoff's law, the emissivity of an object at each wavelength $\varepsilon(\lambda)$ is equal to its absorptivity $\alpha(\lambda)$ under thermal

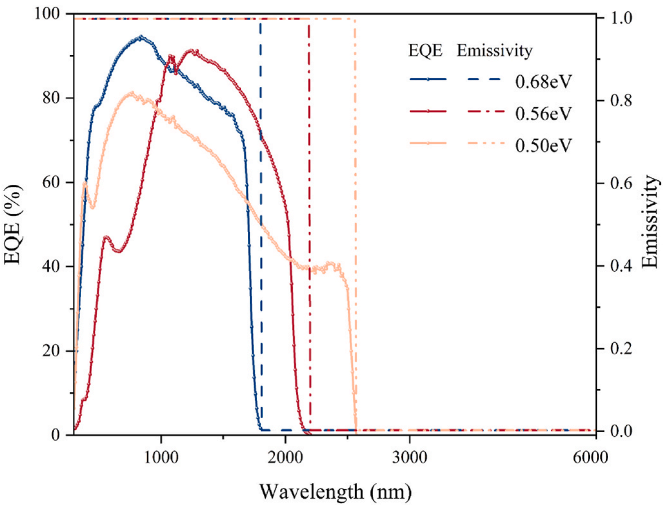

Fig. 1. Quantum efficiency of InGaAs cells with different bandgaps and the corresponding ideal emissivity spectrum of the emitter.

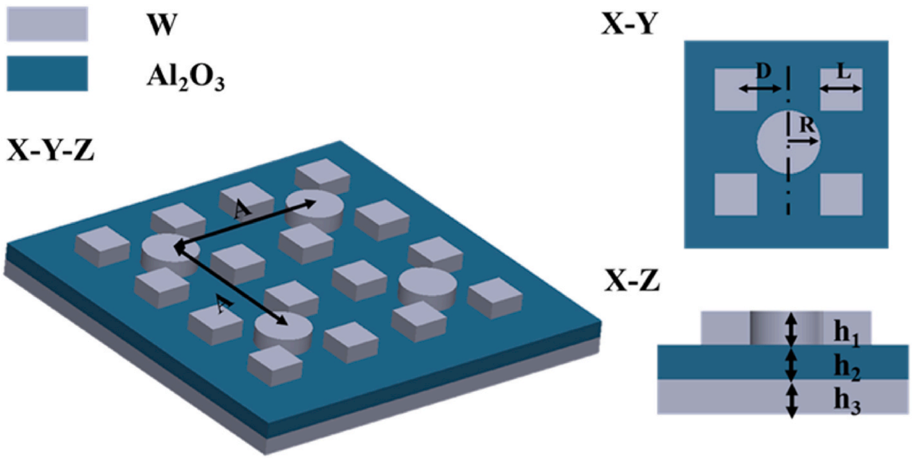

Fig. 2. Model of the hybrid-patterned metasurface emitter.

equilibrium conditions. In addition, given that the metal substrate at the bottom of the hybrid-patterned metasurface emitter is on the order of microns, the transmittance of photons in the wavelength range of 0.3–6.0 μm is regarded as zero. Therefore, the emissivity of the emitter $\varepsilon(\lambda)$ can be calculated using the following equation:

$$\varepsilon(\lambda) = \alpha(\lambda) = 1\text{-}r(\lambda), \tag{1}$$

where λ is the wavelength of the spectrum, $r(\lambda)$ is the reflectance of the object.

The radiant power I_{em} of the emitter can be expressed as:

$$I_{\mathrm{BB}}(\lambda, T) = \frac{2hc^2}{\lambda^5}\frac{1}{e^{\frac{hc}{\lambda k_{\mathrm{B}}T}}\text{-}1}, \tag{2}$$

$$I_{\mathrm{em}} = \varepsilon(\lambda)\, I_{\mathrm{BB}}(\,\lambda, T\,), \tag{3}$$

where $I_{\mathrm{BB}}(\lambda,T)$ is the radiation power of the Blackbody at temperature T, h is the Planck's constant, c is the speed of light in vacuum, and k_{B} is the Boltzmann's constant.

To evaluate the spectral control performance of the emitter, the effective spectral efficiency η_{sp} defined in Ref. [38] was used as the optimization indicator. The specific formula is presented as follows:

$$\eta_{\mathrm{t}} = \frac{\int_0^{\lambda pv} I_{\mathrm{em}}(\lambda, T)d\lambda}{\int_0^{\infty} I_{\mathrm{em}}(\lambda, T)d\lambda}, \tag{4}$$

$$\eta_{\mathrm{c}} = \frac{\int_0^{\lambda_{\mathrm{PV}}} I_{\mathrm{em}}(\lambda, T)d\lambda}{\int_0^{\lambda_{\mathrm{PV}}} I_{\mathrm{BB}}(\lambda, T)d\lambda}, \tag{5}$$

$$\eta_{\mathrm{sp}} = \eta_{\mathrm{t}}\eta_{\mathrm{c}}, \tag{6}$$

where λ_{PV} is the cut-off wavelength of the PV cell, η_{t} is the proportion of photons shorter than the λ_{PV} in the emission spectrum of the emitter, which indicates the degree to which in-band thermal radiation energy can be suppressed, and η_{c} is the proportion of the thermal radiation spectrum of the emitter within λ_{PV} to that of the blackbody thermal radiation spectrum, which measures the intensity of the in-band emission of the emitter.

2.2. *Inverse design of emitters*

Neural networks and genetic algorithms were utilized to predict and optimize the structure of emitters. Forward and inverse neural network models were constructed in PyTorch, which is an open-source deep learning framework that provides flexible and efficient tools for building and training neural networks. In the forward model, structural parameters were input to predict emissivity spectrum, whereas in the inverse model, the target emissivity spectrum was input to predict geometric structures. The outputs of the inverse model are interrelated, as described by Formulas (7) and (8), necessitating the inclusion of penalty term weights into the model to ensure adherence to these physical constraints.

$$0 < R + L \le A, \tag{7}$$

$$\frac{\sqrt{2}R + L}{2} \le D \le \frac{A\text{-}L}{2}, \tag{8}$$

The performance of neural networks is greatly influenced by the selection of hyperparameters. The Optuna tuning tool was utilized to determine the optimal combination of hyperparameters for the neural network. Optuna is a Python library for hyperparameter optimization that provides an automated approach to search for the optimal combination of hyperparameters to improve model performance. This study aimed to minimize the mean squared error (MSE) between the actual and predicted values and to optimize the performance of the forward and inverse models by seeking the optimal combination of hyperparameters.

A genetic algorithm was further applied to optimize the structural parameters predicted by the inverse model. The specific step is shown in Fig. 3. Initially, the inverse model receives the target spectrum as input and outputs the predicted structural parameters. These predicted parameters are then provided to the genetic algorithm, where an initial population is generated by introducing random perturbations to obtain structural parameters near the predicted values. Afterward, these parameters are input into the forward model to generate the response spectrum. The MSE between the response spectrum and the target spectrum is used as the fitness function. Individuals that are closest to the target spectrum are selected and undergo crossover and mutation to iteratively optimize the structural parameters. Finally, the individual with the highest fitness and its structural parameters are output.

2.3. *Modeling of thermophotovoltaic*

When radiation particles impinge on the surface of the InGaAs cell, the output current density $J(V)$ of the InGaAs cell can be calculated in

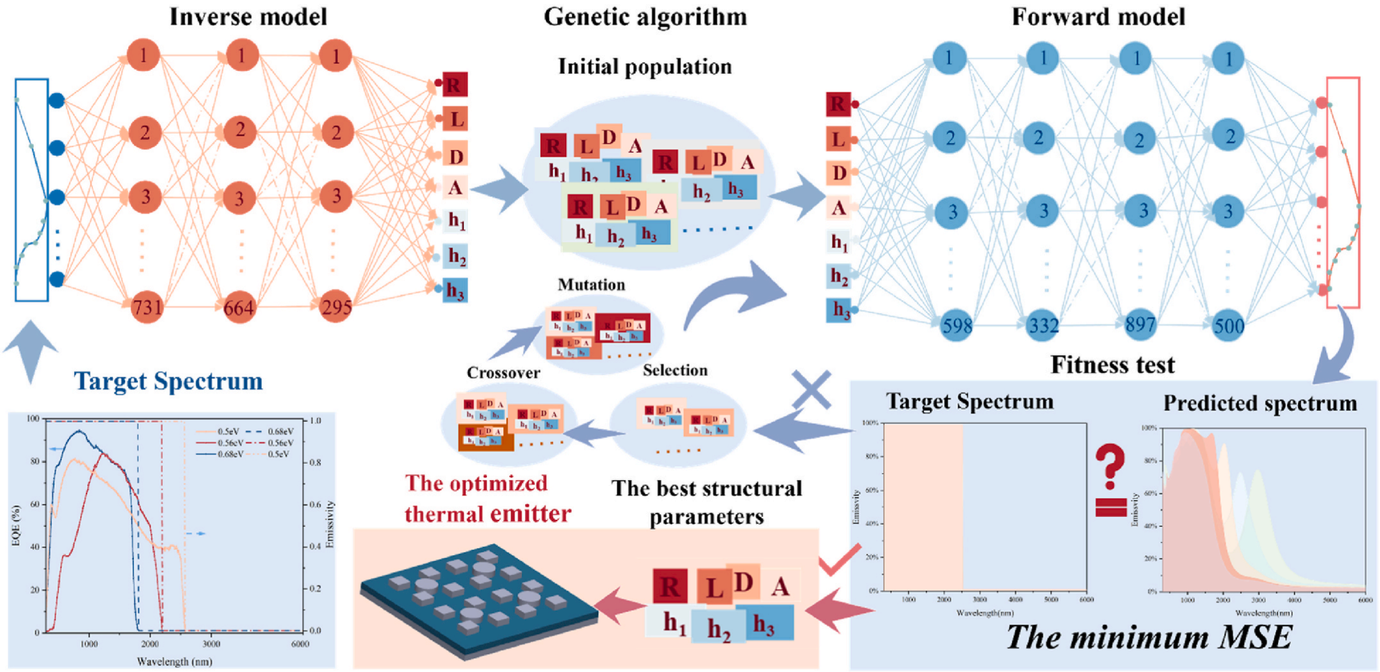

Fig. 3. Specific steps of the neural network inverse design and genetic algorithm optimization for the emitter.

accordance with the Shockley formula. The specific calculation formulas are as follows:

$$J_{SC} = q\int_0^\infty \frac{q\lambda}{hc} QE(\lambda) I_{em}(\lambda, T) d\lambda, \tag{9}$$

$$J_0 = q\int_{E_g}^\infty \frac{2\pi E^2}{h^3c^3\left[\exp\left(\frac{E}{k_B T_a}\right)\text{-}1\right]} dE, \tag{10}$$

$$J(V) = J_{sc}\text{-}J_0\left[\exp\left(\frac{qV}{k_B T_a}\right)\text{-}1\right], \tag{11}$$

where J_{sc} and J_0 represent the short-circuit current density and inverse saturation current density of the InGaAs cell respectively, V is the output voltage, q is the elementary charge, $QE(\lambda)$ is the quantum efficiency of the InGaAs cell, E_g is the bandgap of the InGaAs cell, and T_a = 300 K represents the ambient temperature of the InGaAs cell.

The output power P_{max} and the energy conversion efficiency η_{sys} of the RTPV system can be calculated as follows:

$$P_{max} = \text{Max}(V \times J), \tag{12}$$

$$\eta_{sys} = \frac{P_{max}}{\int_0^\infty I_{em}(\lambda, T) d\lambda}. \tag{13}$$

2.4. Fabrications of emitters

As shown in Fig. 4, the manufacturing process of the hybrid-patterned metasurface emitter is as follows: (1) A silicon (Si) substrate was cleaned using an RCA cleaning station to remove potential organic contaminants, metal ions, and microscopic particles from its surface; (2) A 135 nm-thick W nanolayer was deposited onto the 500 μm-thick Si substrate under vacuum conditions using an electron beam deposition system (DE Technology DE400); (3) A 110 nm-thick Al_2O_3 nanolayer was formed on the W nanolayer using an atomic layer deposition system (Picosun™ R-200 Adv Thermal LC) by alternately introducing precursor molecules (trimethylaluminum, TMA) and reactant molecules (H_2O);

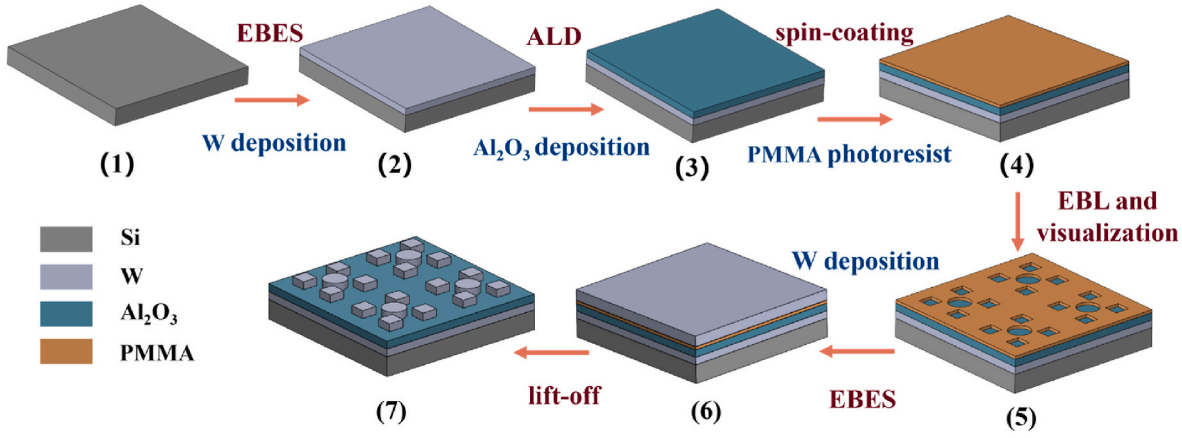

Fig. 4. Fabrication process of the hybrid-patterned metasurface emitter.

(4) A polymethyl methacrylate (PMMA) resist layer was spin-coated onto the Al_2O_3 layer using a spin coater (KW-4A); (5) Circular-square hybrid patterns with a radius of 175 nm, a side length of 246 nm, a spacing of 315 nm, and a periodicity of 1300 nm were exposed onto the PMMA photoresist using an electron beam lithography machine (NanoBeam Limited nB5) with a 0.8 nA beam current. A developer solution composed of methyl isobutyl ketone and isopropanol mixed at a ratio of 3:1 was used to remove the chemically broken regions of the photoresist after exposure, while preserving the mask patterns in the unexposed areas; (6) A 120 nm-thick W nanolayer was deposited again using the electron beam deposition system (DE Technology DE400); (7) The PMMA photoresist was dissolved via ultrasonic cleaning in acetone, assisted by oxygen plasma treatment, to lift off the overlying thin film material. This step left only the patterned material deposited directly on the exposed Al_2O_3 layer, forming the desired metasurface structures.

2.5. Measurements of optical and electrical properties

The morphology of the emitter was characterized using a focused ion beam scanning electron microscope (SEM, CrossBeam 350). The reflectance of the emitter in the wavelength range of 300–2500 nm was measured using a QE-R measurement system (FYL-YS-50LK) and a near-infrared spectrometer (NIR 2500). For the 2500–6000 nm, reflectance was evaluated by the Fourier transform infrared spectrometer (Nicolet™ iS50). Fig. 5 shows the electrical test system of the InGaAs cell. The RTPV system consists of an equivalent heat source, emitters, InGaAs cells, and heat sinks. A programmable linear DC power supply was used to provide energy to the equivalent heat source, creating a high-temperature environment for the emitter to reach the preset target temperature. The output power of the InGaAs cell was measured by the parameter analyzer (Keithley 4200 SCS) at a normal temperature of 293 K and standard atmospheric pressure of 1 atm.

3. Numerical results

3.1. Machine learning optimization results

To evaluate whether the hybrid-patterned metasurface meets the requirements of existing PV cells, the emissivity spectra of the emitters were simulated using the FDTD method with varying structural parameters, as shown in Fig. 6. In Fig. 6(a), the cut-off wavelength of the spectrum increases with the increase in parameters R. When R is 300 nm, the cut-off wavelength extends to approximately 4000 nm, which remarkably exceeds the requirement for matching the cutoff wavelength of the response band of current PV cells. With R fixed at 170 nm, the parameters L, A, and D primarily influence the emissivity of the emitter in the 300–2000 nm (Fig. 6b–d). These results indicate that the hybrid-patterned metasurface, with carefully optimized structural parameters, can meet the demands for broadband, high-response performance in the specific spectral bands of existing PV cells.

A dataset of 1602 sets of structure-spectrum was obtained using FDTD simulation. After 1000 hyperparameter combinations with the Optuna tuning tool, the optimal parameters for the forward model were obtained at the minimum MSE of 0.0013, whereas the optimal parameters for the inverse model were obtained at the minimum MSE of 0.0046 (Table 1). These optimal hyperparameters were then used to construct both the forward and inverse models.

Table 2 presents the predicted structures optimized for the ideal spectrum matching with 0.68 eV, 0.56 eV, and 0.50 eV InGaAs cells, along with their corresponding effective spectral efficiency η_{sp} at 1300 K. The η_{sp} of these designed emitters exceeds 50%, increasing further with higher bandgap values. These results indicate that reasonable structure parameters of the hybrid-patterned metasurface enable the emitter to significantly enhance photon emission before the cut-off wavelength, while effectively suppressing photon emission beyond the cut-off wavelength.

Fig. 7(a–c) illustrate the comparison between the predicted spectra output by the forward model and the spectra simulated by FDTD. The results show that the predicted spectra are in agreement with the

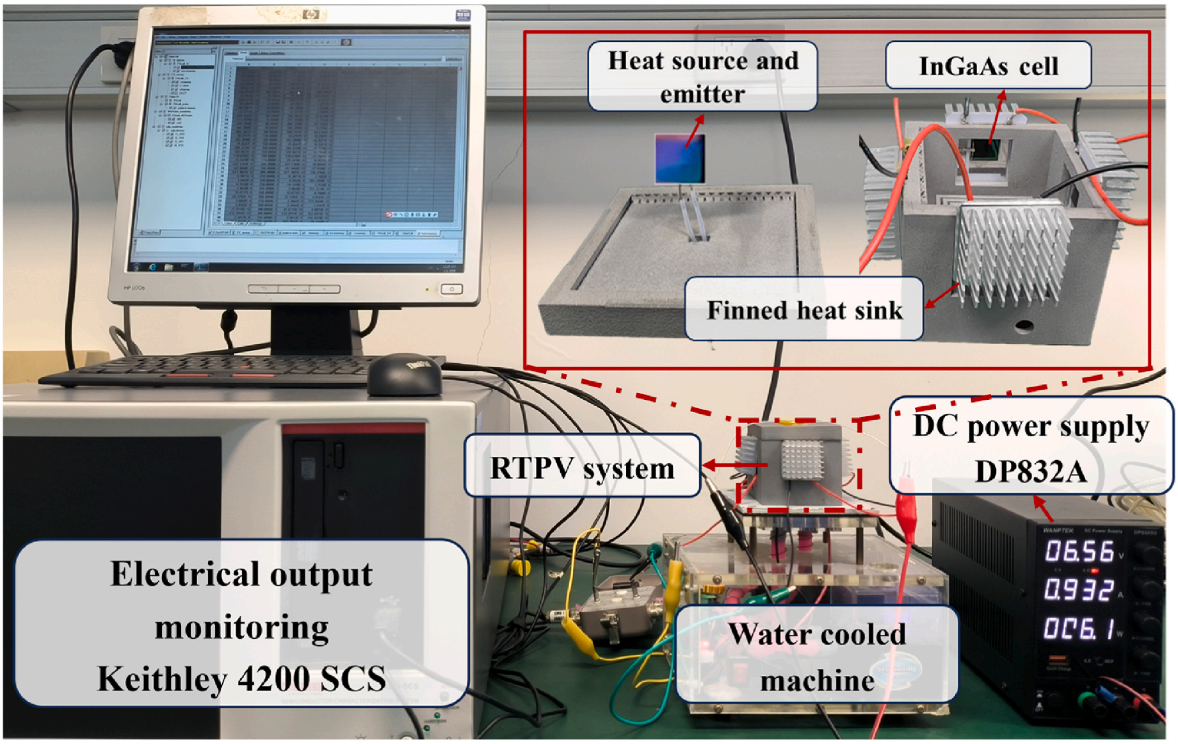

Fig. 5. Electrical test system of the InGaAs cell.

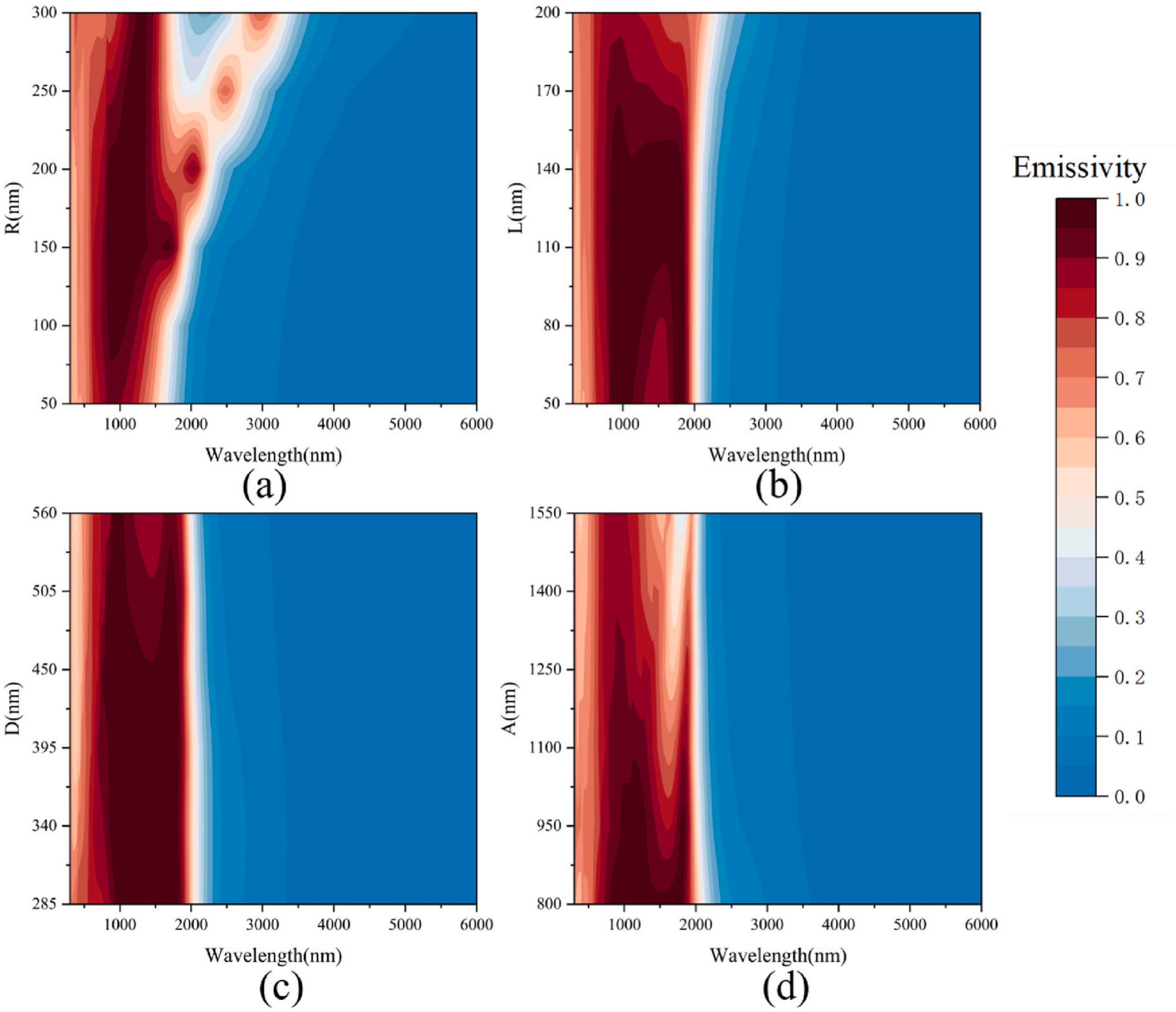

Fig. 6. Emissivity spectrum of the hybrid-patterned metasurface emitter at different parameters: (a) *R*, (b) *L*, (c) *D*, and (d) *A*.

Table 1
Parameter selection for forward and inverse models.

Type	Forward model	Inverse model
Network Architecture	7-598-332-897-263-500	500-731-664-295-7
Optimizer	Adam	RMSprop
Activation Function	ReLU	ReLU
Learning rate	0.0015	0.000389
Dropout	0.01078	0.0634
Batch size	75	125
momentum	\	0.9676
Weight decay	1.032e-05	\
Penalty weight	\	1.0009e-06
MSE	0.0013	0.0046

Table 2
The predicted structural parameters and η_{sp} of the hybrid-patterned metasurface emitter.

E_g (eV)	Structural parameter (nm)							η_{sp}
	R	*L*	*A*	*D*	h_1	h_2	h_3	
0.68	115	136	744	210	100	90	126	51.38%
0.56	175	246	1300	315	120	110	135	69.84%
0.50	219	252	1380	373	95	91	154	71.05%

simulated spectra, with errors less than 0.0027. Furthermore, the emissivity spectrum of the designed emitter can meet the response requirements of their respective cells, with high in-band broadband emission and near-zero out-of-band emission. As shown in Fig. 7(d), the designed emitter exhibits the highest η_c at $E_g = 0.56$ eV, with η_{sp} differing by no more than 2% compared with $E_g = 0.50$ eV. Therefore, considering both η_{sp} and the influence of bandgap on open circuit voltage, further research will focus on evaluating the performance of the designed emitter to match the response band of 0.56 eV InGaAs cells.

3.2. Optical and electrical properties

The emissivity spectrum and η_{sp} for the designed emitter were compared with those of planar W, nickel oxide-doped magnesium oxide in Ref. [11], and the metasurface emitter in Ref. [24] (Fig. 8). Compared with other types of emitters, the designed emitter exhibits the best emissivity spectrum, with the highest average emission rate occurring before $\lambda_{PV} = 2200$ nm. In particular, the peak in-band emission can reach 99%, and the average in-band emission exceeds 90%. As shown in Fig. 8(b), the η_{sp} of emitters increases with the increase of temperature from 700 K to 1300 K. At the same temperature, the designed emitter exhibits higher η_{sp}. At 1300 K, the designed emitter achieves a η_{sp} of 69.84%, representing 48.24% improvement compared with the planar W. These results indicate that the outstanding spectral control performance of the designed emitter.

Fig. 9 shows the radiation power of the designed emitter and

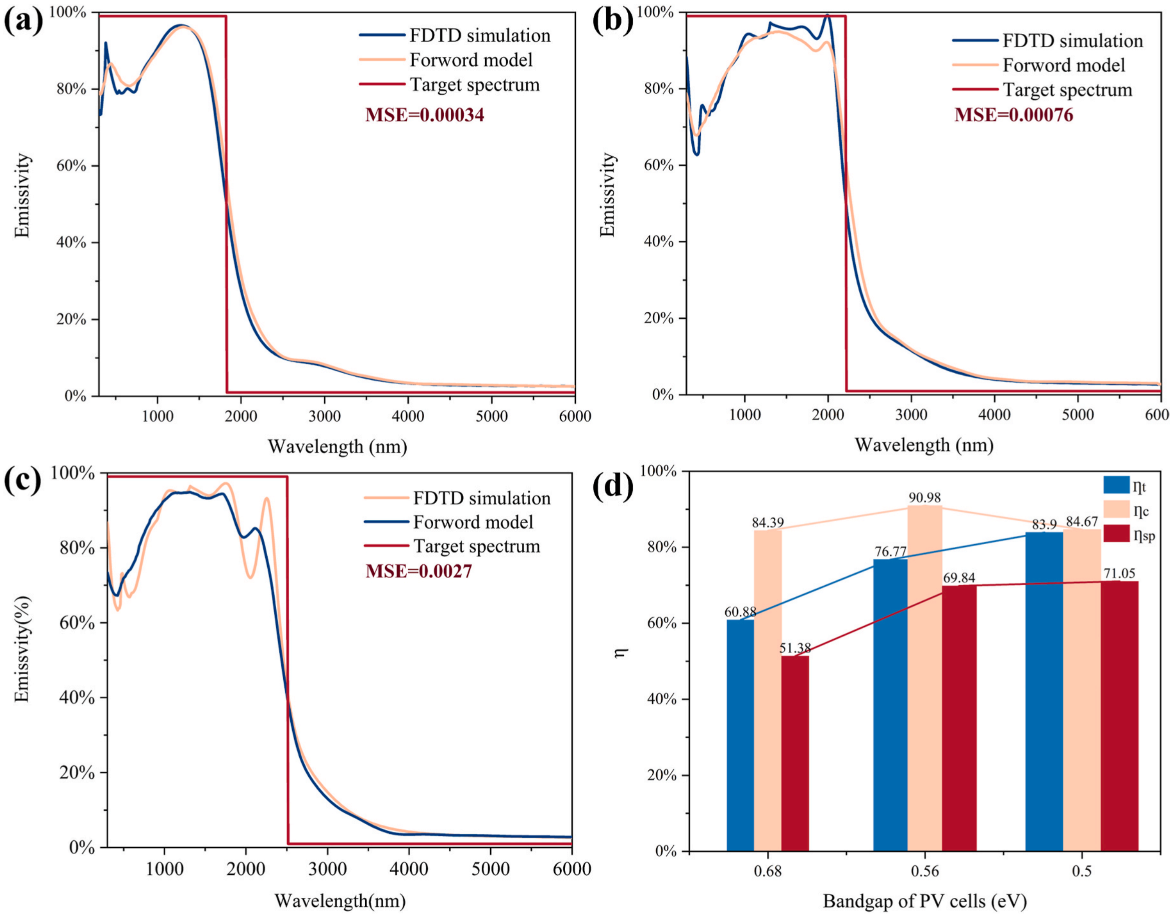

Fig. 7. Emissivity spectrum for the predicted hybrid-patterned metasurface emitters matching the response band of (a) 0.68 eV, (b) 0.56 eV, and (c) 0.50 eV InGaAs cells. (d) η_t, η_c, and η_{sp} of the designed emitters for InGaAs cells with different bandgaps.

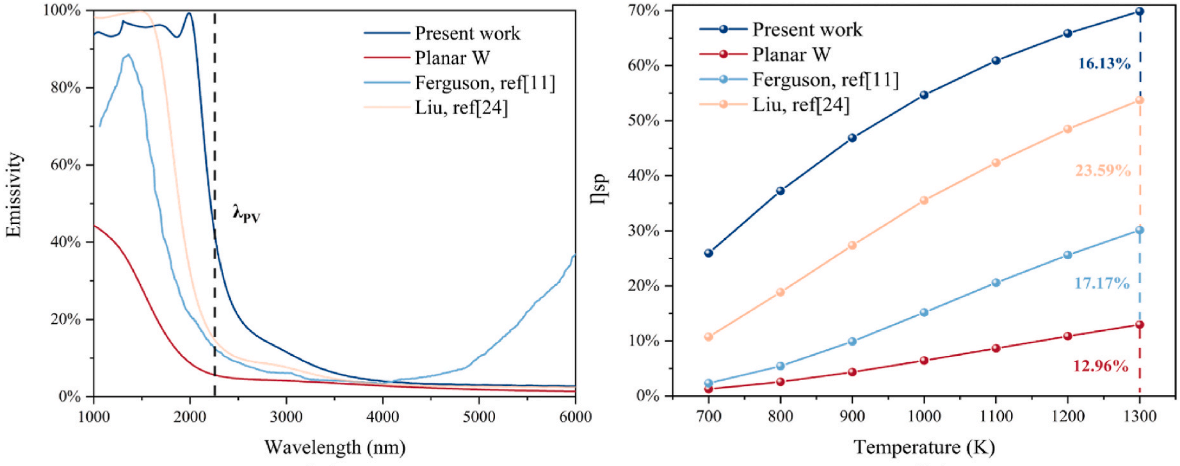

(a) (b)

Fig. 8. (a) Emissivity spectrum, and (b) η_{sp} for the present work, planner W, nickel oxide-doped magnesium oxide and metasurface emitter.

blackbody at different temperatures. As the temperature increases, the peak of the radiation spectrum gradually shifts toward shorter wavelengths, which is within the optimal matching range of the 0.56 eV InGaAs cell. The designed emitter exhibits selective thermal radiation. The in-band radiation power $P_{\text{in-band}}$ of the designed emitter is close to that of the blackbody for wavelengths shorter than λ_{PV}. The out-of-band radiation power $P_{\text{out-of-band}}$ maintains a low level for wavelengths longer than λ_{PV}.

Based on the radiation power spectrum of the emitter with the quantum efficiency of the InGaAs cell, the output performance, $P_{\max}$, and η_{sys} of the system were calculated (Fig. 10). Compared to other types of emitters, the system with the designed emitter demonstrates better output performance, with higher $P_{\max}$ and η_{sys}. At 1300 K, the $P_{\max}$ reaches 1.16 W/cm^2, with the η_{sys} of 20.77%. The designed emitter

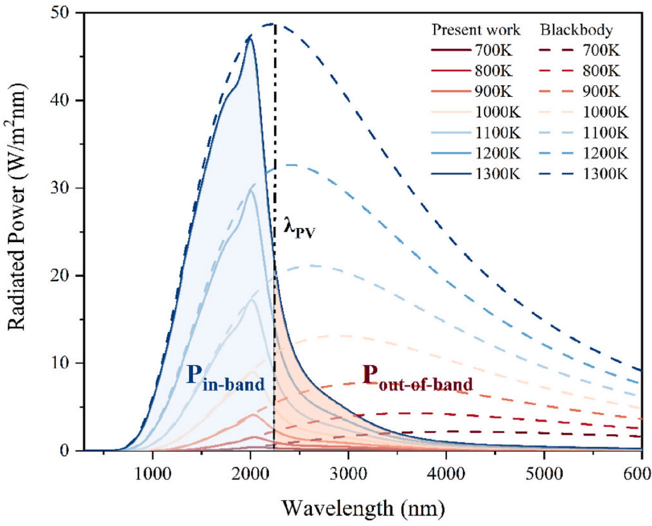

Fig. 9. Radiant power spectrum of the designed emitter and Blackbody.

results in an increase of 0.97 W/cm^2 in $P_{\max}$ and a 6.3% improvement in η_{sys} compared with planar W. This result indicates that the designed emitter enhances the performance of RTPV systems.

Fig. 11 shows the comparison of the $P_{\max}$ and η_{sys} of the RTPV system with and without one-dimensional Si/SiO$_2$ photonic crystal filter at different temperatures. The filter suppresses the generation of unusable photons, though it also partially inhibits useable photons. Compared to the system without the filter, the system with the filter shows an increase in η_{sys} but a decrease in $P_{\max}$. At 1300 K, the $P_{\max}$ of the RTPV system with the filter reduces by 0.36 W/cm^2. The η_{sys} increases to 26.21%, which represents a 5.44% improvement compared to that without the filter. This result indicates that the designed emitter will further enhance η_{sys}, when used in conjunction with the selective filter.

3.3. Polarization and angle insensitivity

In practical RTPV systems, it is essential for the emitter to maintain selective emission characteristics at different incident angles to ensure efficient energy conversion. Fig. 12 shows the performance of the designed emitter for different polarization lights and incident angles. The emissivity spectrum of the designed emitter is unaffected by p-polarization and s-polarization lights, demonstrating polarization insensitivity (Fig. 12(a)). This polarization independence is attributed to the symmetrical design of circular and square patterns within the periodic structure, which ensures consistent electromagnetic field distribution across different polarization states. As shown in Fig. 12(b), the designed emitter maintains high in-band emission and low out-of-band emission characteristics within an incident angle range of 0°–60°, with minimal variation in emissivity at different wavelengths. This angle insensitivity is primarily attributed to the periodic metasurface, which enables uniform interaction with incident light at various angles and induces Bragg scattering effects, thereby contributing to a stable spectral response. Consequently, the designed hybrid-patterned metasurface emitters maintains selective emission across a wide range of angles, ensuring its efficient operation of the emitter in practical RTPV applications.

3.4. Electromagnetic field analysis

To understand the emission enhancement mechanism, electromagnetic field distributions in the x-z section of the hybrid-patterned metasurface emitter at $\lambda = 1.30$ μm or 1.99 μm (high emissivity) and $\lambda = 4.00$ μm (low emissivity) are shown in Fig. 13. The difference in emissivity at different wavelengths is due to variations in the distribution of local electric and magnetic fields in the emitter. The local electric field is primarily distributed near the W surface and the local magnetic field is

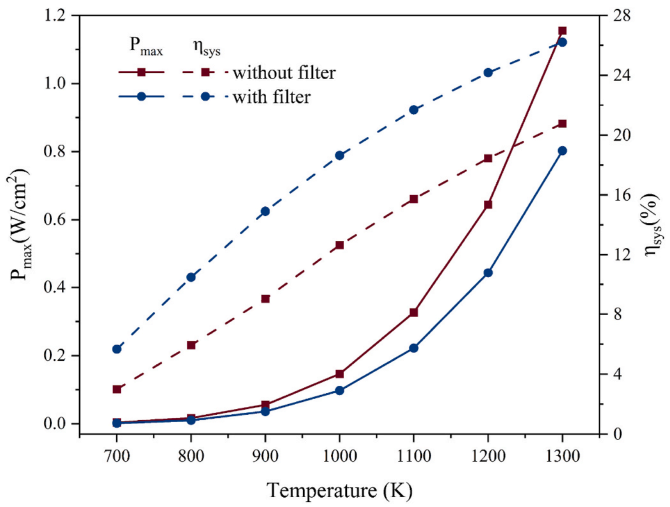

Fig. 11. Maximum output power density $P_{\max}$ and energy conversion efficiency η_{sys} with and without the filter at different temperatures.

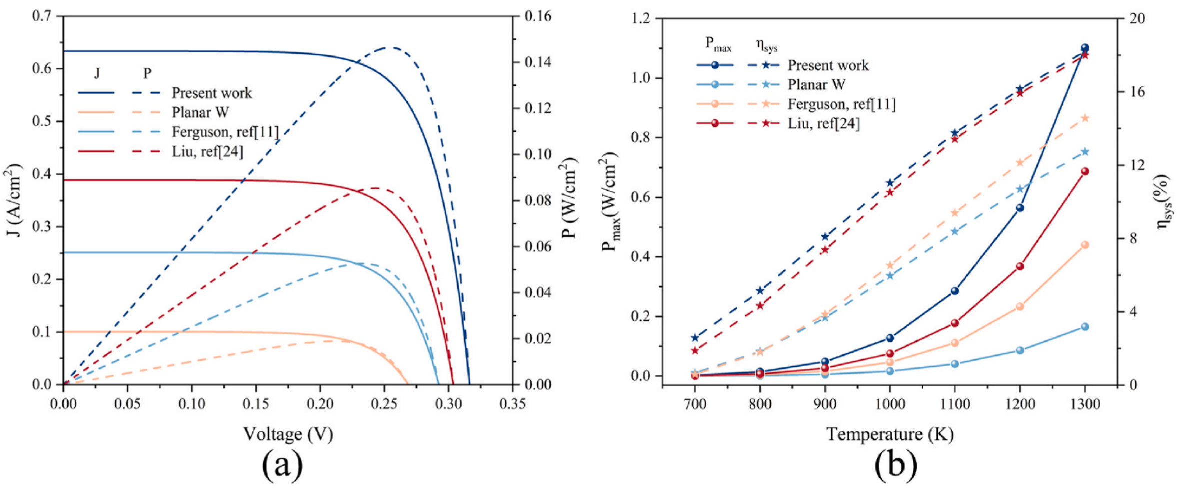

Fig. 10. (a) Output performance of the 0.56 eV InGaAs cell at 1000 K with different emitters. (b) Maximum output power density $P_{\max}$ and energy conversion efficiency η_{sys} for the application of different emitter systems.

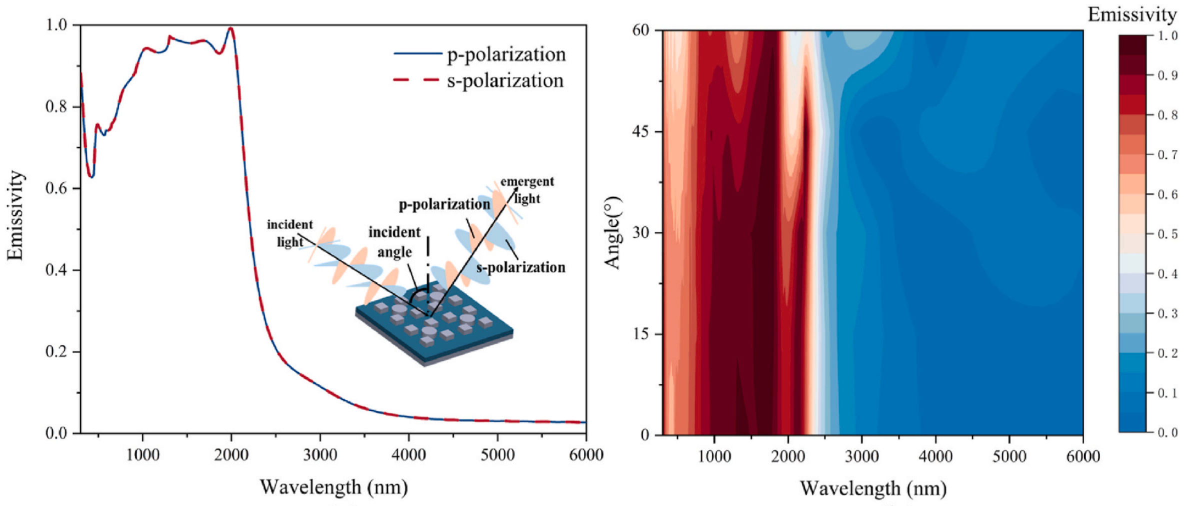

(a) (b)

Fig. 12. Emissivity spectra of the hybrid-patterned metasurface emitter for (a) different polarizations, and (b) various incident angles.

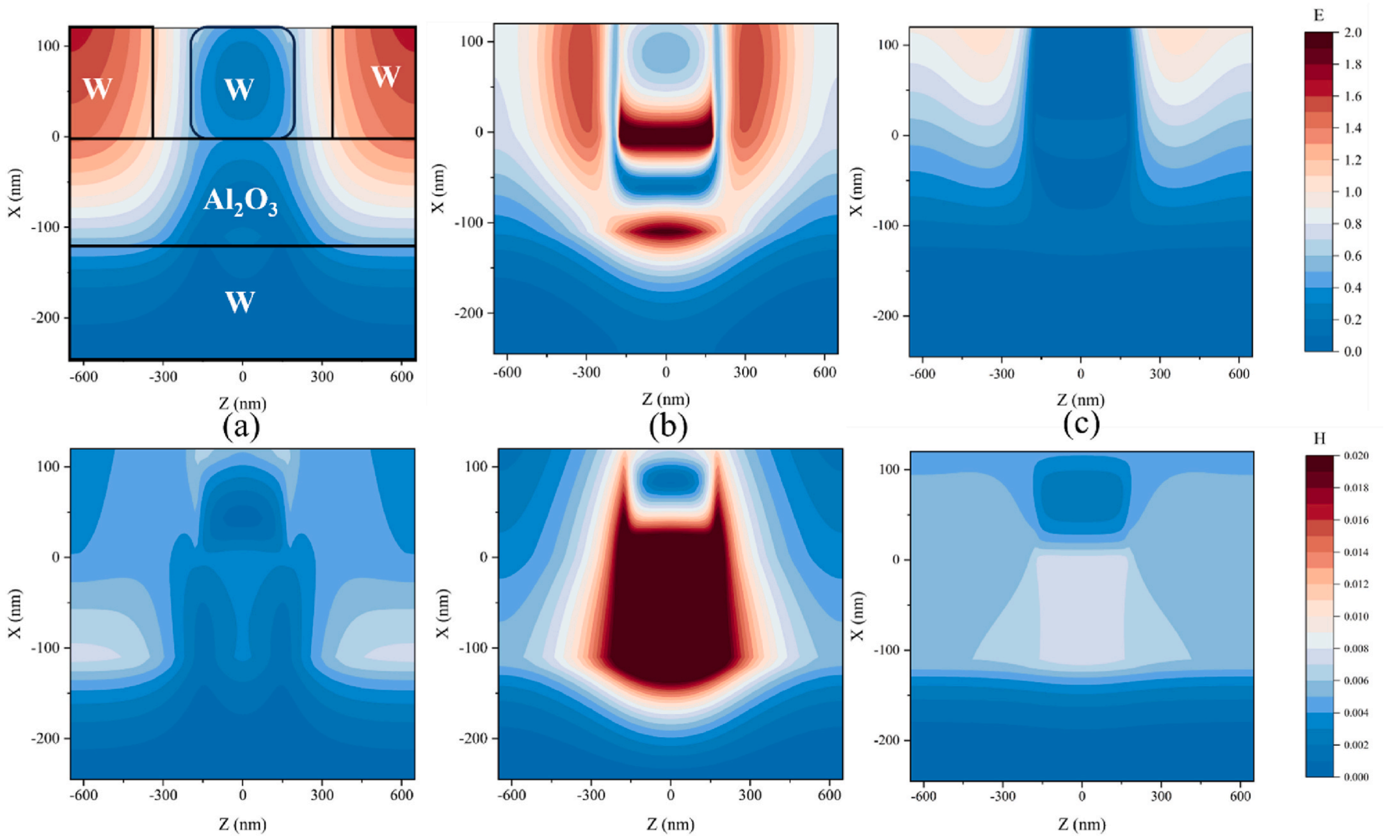

(a) (b) (c)

(d) (e) (f)

Fig. 13. Electric field distribution for (a) $\lambda = 1.30$ μm, (b) $\lambda = 1.99$ μm, and (c) $\lambda = 4.00$ μm and magnetic field distribution for (d) $\lambda = 1.30$ μm, (e) $\lambda = 1.99$ μm, and (f) $\lambda = 4.00$ μm in the x–z section of the hybrid-patterned metasurface emitter.

mainly located in the dielectric layer. When the electromagnetic wave of a specific wavelength is incident on the interface between the metal and the dielectric, the coupling of the metal surface charge and the electromagnetic wave undergoes collective oscillation. This movement is characterized by the fact that the electric field is mainly distributed in the vicinity of the metal. $\lambda = 1.30$ μm can be mainly attributed to surface plasmon excitation. When dielectric materials interact with electromagnetic waves, electrons or particles possessing magnetic moments within the dielectric material undergo resonance. The electric field is mainly distributed near the dielectric. Therefore, the enhancement of the emission at $\lambda = 1.99$ μm can be attributed to the co-excitation of surface plasmons and magnon polaritons. The high-emissivity peaks of the emitter primarily result from the combined response of the aforementioned mechanisms. By adjusting the structural parameters, the hybrid-patterned metasurface emitter can couple different plasma modes, thereby enhancing spectral emissivity peaks within the target bandwidth.

4. Experiment result

4.1. Characterizations of emitters

The hybrid-patterned metasurface emitter was successfully fabricated using advanced micro-nano manufacturing technology. As shown in Fig. 14, the diameter of the circle pattern $2R$ is 352.8 nm, with a deviation of 0.8% from the designed value. The side lengths of the square patterns L are 247.9 nm and 250.1 nm, with relative deviations from the design values less than 2%. The period of the hybrid pattern A is 1.306 μm, with a relative deviation from the design value of less than 0.5%. All the patterns exhibit highly periodic arrangements, and the metasurface structure is in agreement with the simulated design parameters. However, some areas near patterns exhibit incomplete removal of the W layer. Overall, this demonstrates that the employed fabrication technology can precisely produce the required design patterns, thereby providing a solid foundation for the application of metasurface emitters.

4.2. Optical and electrical properties

The emissivity of the hybrid-patterned metasurface emitter at different wavelengths is shown in Fig. 15 (a). The hybrid-patterned metasurface emitter exhibits an average emissivity exceeding 85% in the 300–2200 nm, which is higher than that of planar W. Furthermore, the emissivity decreases sharply and approaches zero at $\lambda_{PV} > 2200$ nm. As shown in Fig. 15 (b), the $P_{\max}$ of the InGaAs cell with the hybrid-patterned metasurface emitter exceeds that of planar W emitter at temperatures ranging from 900 K to 1100 K. Specifically, the $P_{\max}$ can reach 35.86 mW/cm^2 at 1100 K, which is 1.69 times higher than that of the planar W emitter. The experimental results demonstrate that the fabricated hybrid-patterned metasurface emitter possesses selective emission characteristics. This enables more efficient conversion of thermal energy into photon energy that can be utilized by the InGaAs cell, thereby enhancing the $P_{\max}$ of the system.

Nevertheless, discrepancies were observed between the experimental and simulated results, which can be attributed to several factors. Firstly, the simulation assumed that all useable thermal radiation generated by the emitter was fully absorbed and converted into electrical energy by the InGaAs cell, with the cell operating at a constant temperature of 300 K. However, these assumptions do not fully capture the complexity of practical systems, such as thermal losses, material aging, and other environmental factors. Additionally, in the current experimental setup, simple heat sinks were used, which were not effective in managing the thermal load. This limitation resulted in performance degradation due to elevated temperature effects. Therefore, future research should explore more advanced thermal management solutions to reduce the influence of temperature on performance of the InGaAs cell. Lastly, the instability of the emitter at high temperatures affects the electrical output. To address this, future designs could investigate high-temperature-resistant coatings (hafnium oxide) to enhance the emitter's resistance to oxidation and diffusion, ensuring the performance of emitter remains stable under high temperatures. We believe that by addressing these challenges, the gap between experimental and simulated results will be narrowed.

5. Conclusion

This study proposes a method that combines a deep learning inverse design with genetic algorithms to optimize hybrid-patterned metasurface emitters. The predicted spectrum of the designed emitters matches the actual spectrum with an error of less than 0.0027. The designed emitter, which matches the response band of 0.56 eV InGaAs cells, exhibits over 90% in-band emission and near-zero out-of-band emission.

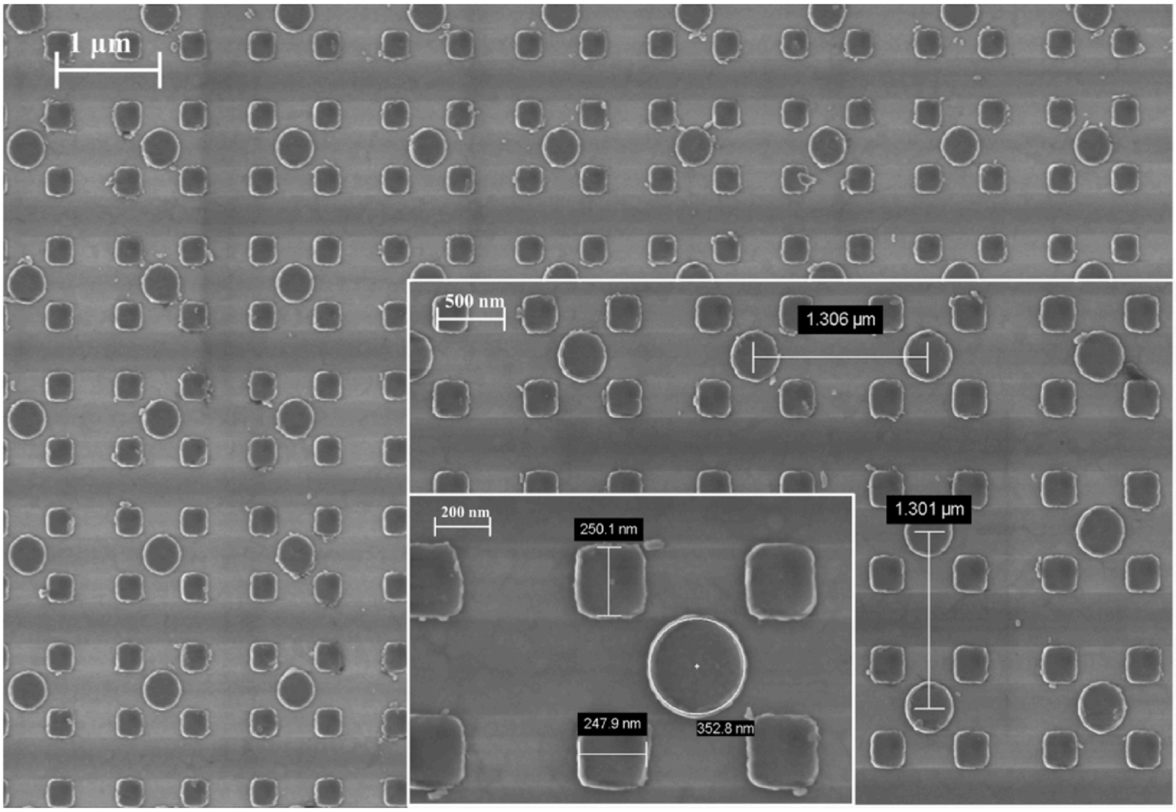

Fig. 14. SEM image of the hybrid-patterned metasurface emitter.

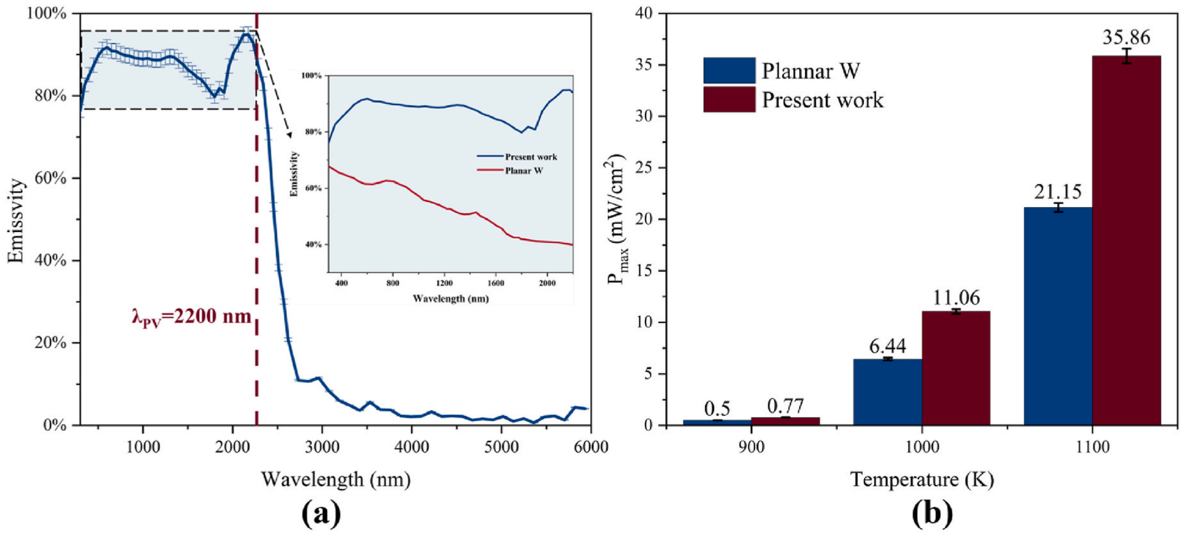

Fig. 15. (a) Emissivity spectrum of the hybrid-patterned metasurface emitter and planar W. (b) P_{max} of the InGaAs cell with different emitters.

Broadband emission enhancement results from the combined response of surface plasmons and magnon polaritons. Moreover, the designed emitter maintains selective emission characteristics under different polarizations and incident angles up to 60°. The RTPV system consists of the designed emitter and InGaAs cells show excellent performance when the temperature of the emitter reaches 1300 K. Compared with planar W emitter, the designed emitter demonstrates an increase of 56.77% in effective spectral efficiency, a 0.97 W/cm^2 increase in the maximum output power density of the InGaAs cell, and a 6.3% improvement in energy conversion efficiency. When the designed emitter used in conjunction with one-dimensional Si/SiO$_2$ photonic crystal filter, the energy conversion efficiency can be further increased to 26.21%. The experimental results prove that the hybrid-patterned metasurface emitter can precisely fabricated by advanced micro-nano manufacturing technology. The emitter exhibits an average emissivity exceeding 85% in the 300–2200 nm. And the maximum output power density of the RTPV system can reach 35.86 mW/cm^2 at 1100 K. This study demonstrates the efficient design and fabrication of the hybrid-patterned metasurface emitter with selective emission characteristics, which has potential applications in thermal radiation engineering. Future work could focus on advanced thermal management solutions and improving emitter stability to enhance the experimental performance of the TPV system.

CRediT authorship contribution statement

Ting Cai: Writing – original draft, Software, Methodology, Formal analysis, Data curation. **Zhiheng Xu:** Writing – review & editing, Supervision, Methodology, Funding acquisition, Formal analysis. **Yujie Yi:** Software, Formal analysis. **Chen Wang:** Writing – review & editing, Visualization. **Baisong Zhou:** Validation, Methodology. **Chao Chen:** Writing – review & editing, Conceptualization. **Yunpeng Liu:** Writing – review & editing, Funding acquisition. **Yuqiao Wang:** Writing – review & editing. **Hongbo Lu:** Writing – review & editing. **Xiaobin Tang:** Writing – review & editing, Supervision.

Declaration of competing interest

The authors declare that they have no known competing financial interests or personal relationships that could have appeared to influence the work reported in this paper.

Acknowledgements

This work is supported by the National Natural Science Foundation of China (Grant Nos. 12275132 and 12075119), the Fundamental Research Funds for the Central Universities (Grant No. NT2023013), and the prospective layout project of Nanjing University of Aeronautics and Astronautics (Grant No. ILB240161A24).

Data availability

Data will be made available on request.

References

[1] R. Sakakibara, V. Stelmakh, W.R. Chan, M. Ghebrebrhan, J.D. Joannopoulos, M. Soljačić, et al., Practical emitters for thermophotovoltaics: a review, J. Photon. Energy 9 (2019) 1, https://doi.org/10.1117/1.JPE.9.032713.

[2] Y. Liu, L. Tang, J. Shao, Y. Tang, J. Li, X. Lv, et al., Experimental performance comparison of 0.72 eV-GaSb and 0.59 eV-InGaAs thermophotovoltaic cells under different radiation temperatures, Appl. Energy 361 (2024) 122959, https://doi.org/10.1016/j.apenergy.2024.122959.

[3] D. Wilt, D. Chubb, D. Wolford, P. Magari, C. Crowley, Thermophotovoltaics for space power applications, AIP Conf. Proc. 890 (2007) 335–345, https://doi.org/10.1063/1.2711751.

[4] H. Wang, Z. Xu, C. Wang, Z. Hou, M. Bian, N. Zhuang, et al., Optimized design and application performance analysis of heat recovery hybrid system for radioisotope thermophotovoltaic based on thermoelectric heat dissipation, Appl. Energy 355 (2024) 122259, https://doi.org/10.1016/j.apenergy.2023.122259.

[5] S. Ni, D. Zhao, M. Sellier, J. Li, X. Chen, X. Li, et al., Thermal performances and emitter efficiency improvement studies on premixed micro-combustors with different geometric shapes for thermophotovoltaics applications, Energy 226 (2021) 120298, https://doi.org/10.1016/j.energy.2021.120298.

[6] A. Datas, A. Martí, Thermophotovoltaic energy in space applications: review and future potential, Sol. Energy Mater. Sol. Cells 161 (2017) 285–296, https://doi.org/10.1016/j.solmat.2016.12.007.

[7] R.G. Lange, W.P. Carroll, Review of recent advances of radioisotope power systems, Energy Convers. Manag. 49 (2008) 393–401, https://doi.org/10.1016/j.enconman.2007.10.028.

[8] T. Burger, C. Sempere, B. Roy-Layinde, A. Lenert, Present efficiencies and future opportunities in thermophotovoltaics, Joule 4 (2020) 1660–1680, https://doi.org/10.1016/j.joule.2020.06.021.

[9] B. Bitnar, W. Durisch, J.-C. Mayor, H. Sigg, H.R. Tschudi, Characterisation of rare earth selective emitters for thermophotovoltaic applications, Sol. Energy Mater. Sol. Cells 73 (2002) 221–234, https://doi.org/10.1016/S0927-0248(01)00127-1.

[10] W.J. Tobler, W. Durisch, High-performance selective Er-doped YAG emitters for thermophotovoltaics, Appl. Energy 85 (2008) 483–493, https://doi.org/10.1016/j.apenergy.2007.10.006.

[11] L.G. Ferguson, F. Dogan, A highly efficient NiO-Doped MgO matched emitter for thermophotovoltaic energy conversion, Mater. Sci. Eng. B 83 (2001) 35–41, https://doi.org/10.1016/S0921-5107(00)00795-9.

[12] Z. Wang, D. Kortge, Z. He, J. Song, J. Zhu, C. Lee, et al., Selective emitter materials and designs for high-temperature thermophotovoltaic applications, Sol. Energy

Mater. Sol. Cells 238 (2022) 111554, https://doi.org/10.1016/j.solmat.2021.111554.

[13] M. Laroche, C. Arnold, F. Marquier, R. Carminati, J.-J. Greffet, S. Collin, et al., Highly directional radiation generated by a tungsten thermal source, Opt. Lett. 30 (2005) 2623–2625, https://doi.org/10.1364/OL.30.002623.

[14] J.I. Watjen, X.L. Liu, B. Zhao, Z.M. Zhang, A Computational simulation of using tungsten gratings in near-field thermophotovoltaic devices, J. Heat Tran. 139 (2017), https://doi.org/10.1115/1.4035356.

[15] K. Cui, P. Lemaire, H. Zhao, T. Savas, G. Parsons, A.J. Hart, Tungsten–carbon nanotube composite photonic crystals as thermally stable spectral-selective absorbers and emitters for thermophotovoltaics, Adv. Energy Mater. 8 (2018) 1801471, https://doi.org/10.1002/aenm.201801471.

[16] I. Celanovic, F. O'Sullivan, M. Ilak, J. Kassakian, D. Perreault, Design and optimization of one-dimensional photonic crystals for thermophotovoltaic applications, Opt. Lett. 29 (2004) 863–865, https://doi.org/10.1364/OL.29.000863.

[17] S.Y. Lin, J. Moreno, J.G. Fleming, Three-dimensional photonic-crystal emitter for thermal photovoltaic power generation, Appl. Phys. Lett. 83 (2003) 380–382, https://doi.org/10.1063/1.1592614.

[18] C. Meng, Y. Liu, Z. Xu, H. Wang, X. Tang, Selective emitter with core–shell nanosphere structure for thermophotovoltaic systems, Energy 239 (2022) 121884, https://doi.org/10.1016/j.energy.2021.121884.

[19] H. Zhang, C. Wang, Y. Shu, J. Liu, K. Ren, F.-Q. Dou, Tunability of a broad-band selective metamaterial emitter in thermophotovoltaic systems, Int. J. Heat Mass Tran. 216 (2023) 124583, https://doi.org/10.1016/j.ijheatmasstransfer.2023.124583.

[20] T.C. Huang, B.X. Wang, C.Y. Zhao, A novel selective thermophotovoltaic emitter based on multipole resonances, Int. J. Heat Mass Tran. 182 (2022) 122039, https://doi.org/10.1016/j.ijheatmasstransfer.2021.122039.

[21] M. Chirumamilla, G.V. Krishnamurthy, K. Knopp, T. Krekeler, M. Graf, D. Jalas, et al., Metamaterial emitter for thermophotovoltaics stable up to 1400 °C, Sci. Rep. 9 (2019) 7241, https://doi.org/10.1038/s41598-019-43640-6.

[22] Z. Zhou, C. Jiang, H. Huang, L. Liang, G. Zhu, Three-junction tandem photovoltaic cell for a wide temperature range based on a multilayer circular truncated cone metamaterial emitter, Energy 210 (2020) 118503, https://doi.org/10.1016/j.energy.2020.118503.

[23] K. Yuan, B. Chen, S. Shan, J. Xu, Q. Yang, Tunable narrowband metamaterial thermophotovoltaic emitter: ideal performance analysis and structural design based on photovoltaic cell performance matching, Energy Convers. Manag. 312 (2024) 118556, https://doi.org/10.1016/j.enconman.2024.118556.

[24] X.J. Liu, C.Y. Zhao, B.X. Wang, J.M. Xu, Tailorable bandgap-dependent selective emitters for thermophotovoltaic systems, Int. J. Heat Mass Tran. 200 (2023) 123504, https://doi.org/10.1016/j.ijheatmasstransfer.2022.123504.

[25] H.-Y. Pan, X. Chen, X.-L. Xia, A review on the evolvement of optical-frequency filtering in photonic devices in 2016–2021, Renew. Sustain. Energy Rev. 161 (2022) 112361, https://doi.org/10.1016/j.rser.2022.112361.

[26] R. Kumar, M. Kumar, J.S. Chohan, S. Kumar, Overview on metamaterial: history, types and applications, Mater. Today Proc. 56 (2022) 3016–3024, https://doi.org/10.1016/j.matpr.2021.11.423.

[27] N.A. Pfiester, T.E. Vandervelde, Selective emitters for thermophotovoltaic applications, Phys Status Solidi A 214 (2017) 1600410, https://doi.org/10.1002/pssa.201600410.

[28] Y. Tian, X. Liu, A. Ghanekar, Y. Zheng, Scalable-manufactured metal–insulator–metal based selective solar absorbers with excellent high-temperature insensitivity, Appl. Energy 281 (2021) 116055, https://doi.org/10.1016/j.apenergy.2020.116055.

[29] R. Feng, W. Ding, L. Liu, L. Chen, J. Qiu, G. Chen, Dual-band infrared perfect absorber based on asymmetric T-shaped plasmonic array, Opt. Express 22 (2014) A335–A343, https://doi.org/10.1364/OE.22.00A335.

[30] B. Zhang, J. Hendrickson, J. Guo, Multispectral near-perfect metamaterial absorbers using spatially multiplexed plasmon resonance metal square structures, JOSA B 30 (2013) 656–662, https://doi.org/10.1364/JOSAB.30.000656.

[31] X.J. Liu, C.Y. Zhao, B.X. Wang, J.M. Xu, Tailorable bandgap-dependent selective emitters for thermophotovoltaic systems, Int. J. Heat Mass Tran. 200 (2023) 123504, https://doi.org/10.1016/j.ijheatmasstransfer.2022.123504.

[32] Q. Wang, Z. Huang, J. Li, G.-Y. Huang, D. Wang, H. Zhang, et al., Module-level polaritonic thermophotovoltaic emitters via hierarchical sequential learning, Nano Lett. 23 (2023) 1144–1151, https://doi.org/10.1021/acs.nanolett.2c03476.

[33] R. Hu, J. Song, Y. Liu, W. Xi, Y. Zhao, X. Yu, et al., Machine learning-optimized Tamm emitter for high-performance thermophotovoltaic system with detailed balance analysis, Nano Energy 72 (2020) 104687, https://doi.org/10.1016/j.nanoen.2020.104687.

[34] Z.A. Kudyshev, A.V. Kildishev, V.M. Shalaev, A. Boltasseva, Machine-learning-assisted metasurface design for high-efficiency thermal emitter optimization, Appl. Phys. Rev. 7 (2020) 021407, https://doi.org/10.1063/1.5134792.

[35] P. Bohm, C. Yang, A.K. Menon, Z.M. Zhang, Thermophotovoltaic emitter design with a hyper-heuristic custom optimizer enabled by deep learning surrogates, Energy 291 (2024) 130424, https://doi.org/10.1016/j.energy.2024.130424.

[36] Z. Liu, D. Zhu, S.P. Rodrigues, K.-T. Lee, W. Cai, Generative model for the inverse design of metasurfaces, Nano Lett. 18 (2018) 6570–6576, https://doi.org/10.1021/acs.nanolett.8b03171.

[37] W. Ma, Z. Liu, Z.A. Kudyshev, A. Boltasseva, W. Cai, Y. Liu, Deep learning for the design of photonic structures, Nat. Photonics 15 (2021) 77–90, https://doi.org/10.1038/s41566-020-0685-y.

[38] L. Mo, L. Yang, E.H. Lee, S. He, High-efficiency plasmonic metamaterial selective emitter based on an optimized spherical core-shell nanostructure for planar solar thermophotovoltaics, Plasmonics 10 (2015) 529–538, https://doi.org/10.1007/s11468-014-9837-6.